Appl. Phys. A (2015) 120:1149–1157
DOI 10.1007/s00339-015-9294-x

Applied Physics A
Materials Science & Processing

Photogeneration process in bulk heterojunction solar cell based on quaterthiophene and CdS nanoparticles

Aida Benchaabane[1,2] · Zied Ben Hamed[1] · Fayçal Kouki[1,3] · Andreas Zeinert[2] · Habib Bouchriha[1]

Received: 6 April 2015 / Accepted: 15 June 2015 / Published online: 1 July 2015

Abstract In this paper, the blended systems composed of organic oligothiophenes and CdS nanoparticles were investigated through their optical and photoelectrical measurements for their potential applications in photovoltaic devices. The electrical and photoelectrical properties of the devices fabricated with the active layer sandwiched between the metal anode and the metal cathode have been reported. Dependence of the performance of this bulk heterojunction photovoltaic device on their composition has been investigated with respect to charge transport. The organic/inorganic interface area in bulk heterojunction is an important factor in the photovoltaic process. The incorporation of nanoparticles in the polymer matrix, for the purpose to fabricate hybrid inorganic–organic materials, could be a good alternative to enhance the charge generation process of free carriers. The *J*–*V* curves of the quaterthiophene (4T) and hybrid quaterthiophene/cadmium sulfide nanoparticles CdS show the important role played by the nanoparticles for energy conversion improvement. The experimental data were found to be in good agreement with a modified Braun–Onsager model.

✉ Fayçal Kouki
benchaabane.aida@yahoo.fr

[1] Laboratoire de Matériaux Avancés et Phénomènes Quantiques, Faculté des Sciences de Tunis, Université Tunis El-Manar, Tunis, Tunisia

[2] Laboratoire de Physique de Matière Condensée, Faculté des Sciences d'Amiens, Amiens, France

[3] Institut Préparatoire aux Etudes d'Ingénieurs El-Manar, Université Tunis El-Manar, Tunis, Tunisia

1 Introduction

Conjugated oligomers offer promising perspectives in the area of optoelectronics thanks to their high degree of flexibility in "molecular engineering" [1], stability toward oxidation process [2] diversity [3, 4], and low cost [5, 6]. However, one of their main drawbacks in photovoltaic applications is the nature of the photogenerated excitons commonly called Frenkel excitons which are too tightly bound to generate free carries. Conversely, inorganic semiconductors in which photogenerated excitons are of the Wannier type with a binding energy much lower than that of Frenkel ones are much more suitable for photovoltaic conversion. Nevertheless, this class of materials suffers high cost and cumbersome manufacturing process. An alternative solution to take maximum advantage of the two precedents compounds is their combination in hybrid organic/inorganic structures obtained by the incorporation of mineral nanoparticles in an organic matrix [7, 8]. The photogenerated exciton [9], which is an elementary state generated by optical excitation, can be obtained from the resonant interaction of Frenkel–Wannier excitons and should be localized in the organic–inorganic structure [10]. Those hybrid excitons have both Frenkel and Wannier optical properties, they have strong oscillation strength like Frenkel excitons and are delocalized and large-sized like Wannier excitons, and they are also sensitive to external perturbations such as electric and magnetic fields and can promote the development of new optoelectronic technologies, in particular, in the photovoltaic field. Such structures are promising and can provide higher power conversion efficiency than pristine organic materials [11, 12]. The quatertiophene is one of the most interesting oligothiophene materials which offers high-structured, well-defined, and chemically stable compounds. We will use it as a prototype

for systems of linear oligothiophenes with a limited number of double bonds. The same applies to the cadmium sulfide (CdS) nanoparticles that we use as a prototype for systems of mineral nanoparticles with great potential in the applications ranging from OLED to solar cell and biosensing [13]. The nature of the charge or energy processes between the organic compound and mineral nanoparticles depends on the electrical and optical properties of the two materials. The efficiency of these heterojunctions is usually limited by charge recombination phenomena, and the electron transport can also be hindered by surface trap states. These traps can affect the hybrid exciton kinetics in the hybrid organic/inorganic composite [14].

In the present work, we first present a basic optical characterization of both the quaterthiophene (4T) and the CdS nanoparticles. After that, a photoelectrical experimental results and theoretical investigation of the effect of CdS nanoparticles (NPs) incorporation in pristine quaterthiophene (4T) are elucidated.

2 Experimental

2.1 Nanoparticles synthesis

CdS nanoparticles were prepared in reverse micellar systems. The detailed synthesis procedure is described elsewhere [15, 16]. All aqueous solutions were made by using distilled water. Two similar solutions of sodium dodecyl sulfate (SDS) and butan-1-ol in hexane (0.1 M SDS), 50 ml (hexane), and 0.9 M (butan-1-ol)) were prepared, and two micellar solutions were achieved by mixing both 0.36 ml of 0.11 M Na_2S and 0.11 M $Cd(CH3COO)_2{\cdot}2H_2O$. The obtained solutions were mixed together and magnetically stirred at 298 K for 1 h. Next, we added dropwise 0.2 ml of dodecanethiol under vigorous magnetic stirring for 2 h. The formation of the CdS NPs took place by the exchange of the micelle contents in the collision process, leading to the chemical reaction in the water pool nanoreactors [17]. Finally, we obtained a pale yellow powder containing the CdS nanoparticles. The size of CdS nanoparticles was controlled by changing the molar ratio $W = [H_2O]/[SDS]$, where $[H_2O]$ and [SDS] are the molar concentrations of water and dodecyl sulfate, respectively. The variation of W allows the control of the concentrations of the cadmium and sulfur precursor so as to get the same concentrations in the reverse micellar solution [18]. In our case, W was set to 4.

2.2 Photovoltaic cell structure deposition and characterization

The organic host matrix consisted of 30 g/l solution of quaterthiophene purchased from Sigma-Aldrich, in chloroform. From the quaterthiophene stock solution, we prepared two different (4T: %[CdS]) solutions with two different weight ratio percentages 0 and 20 %, respectively. The effective mass concentrations obtained from the fraction of the CdS NPs mass (mNPs) to the total composite mass (mNPs + m4T) are 0 and 0.2. The two obtained mixtures were viscous enough to produce quite thick layers deposited by a spin coating technique using the WS-6400BZ-6NPP/LITE model. The ITO glass substrates and only glass substrates were cleaned using acetone, ethanol, and then dried. After deposition, for optical and electrical measurements, the samples were then dried in an ambient-air oven at 80 °C. A general scheme of the PV cell is shown in Fig. 1.

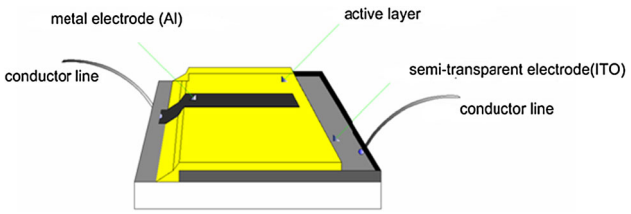

Fig. 1 Photovoltaic cell structure

The photoactive layer, deposited using spin coating, is sandwiched between ITO glass and a 100-nm aluminum electrode deposited by thermal evaporation technique in high vacuum condition ($P = 10^{-6}$ mbar). Morphological characterization was accomplished through AFM microscopy by using Veeco Dimension 3100 AFM (Veeco Digital instruments by Bruker). UV–Vis absorption spectroscopy and UV–Vis fluorescence spectroscopy measurements were taken by a Lambda 12 Perkin-Elmer spectrometer and a Perkin-Elmer MPF-44B spectrofluorimeter, respectively. *J–V* curves have been collected in dark and under illumination by using a Keithley 2400 sourcemeter; the halogen lamp radiation is 10 mW/cm^2 measured with Oriel 68,831 radiometric power supply.

3 Results and discussion

3.1 Optical characterization and size measurement of CdS NPs

The typical absorption spectra and fluorescence spectra of CdS NPs dissolved in THF solution are shown in Fig. 2a. Both absorption and fluorescence extended in UV–Vis range. The first absorption peak is located at 380 nm. Using this value of λ, we deduce the mean size of CdS nanoparticles.

The fluorescence spectrum (Fig. 2b) exhibits the existence of a band located around 430 nm followed by a tail that extends to larger wavelengths. In order to determine

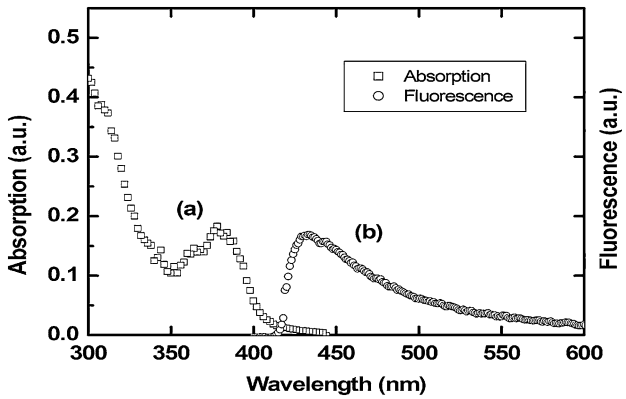

Fig. 2 **a** Absorption and **b** fluorescence spectra of CdS nanoparticles in THF solvent

the size of synthesized CdS nanoparticles, we injected the maximum wavelength absorption λ in the empirical formula given in [19], as expressed:

$$R = \left(-66,521 \times 10^{-8}\right)\lambda^3 + \left(19,557 \times 10^{-4}\right)\lambda^2 - \left(92,352 \times 10^{-2}\right)\lambda + 1329 \quad (1)$$

where R is the radius of the assumed spherical nanoparticles and λ is the wavelength of the first absorption peak. Using the maximum value of absorption $\lambda = 380$ nm, we deduce the mean size R of CdS nanoparticles which is 2.8 nm. This fluorescence spectrum exhibits a broadband which is attributed mainly to the surface trapped energy states. The weak shoulder on the left edge of the emission band can be attributed to the direct band edge recombination [20]. In fact, it is well known that this emission is very sensitive to the nature of nanoparticles surface because of the presence of gap surface states arising from surface non-stoichiometry and unsaturated bonds which can quench the radiative band edge recombination [21].

3.2 Structural characterization of 4T and 4T:20 %[CdS] thin films on glass substrates

The tapping-mode topography AFM images of 4T and 4T/CdS layers are shown in Fig. 3. It can be observed that the nanocomposite surface (Fig. 3b) is rougher than that of the 4T alone (Fig. 3a). The films became less homogeneous and show sever aggregation, and we observed an increase in the grain size and a variation in the thickness of the device [22, 23]. The root-mean-square (RMS) value of pure 4T is 3.61 nm, while that of the 4T:20 %[CdS] film is 10.17 nm; this increase is due to the incorporation of CdS Nps in 4T pristine. Moreover, the larger particles observed in the AFM image can be ascribed to the contribution of the organic capping and/or the formation of clusters from the smaller ones. Indeed, the capping agents may not cover completely the surface of nanoparticles during synthesis and a tendency for further clustering may occur due to electrostatic interactions between particles with different sizes. This clustering reduces the interface between CdS NPs and 4T in the hybrid material [24]. In our case with low ratio concentration, the CdS NPs and the small cluster of CdS NPs are strictly confined in the pores of the 4T pristine [25]. Consequently, one estimates that the percolation and interaction between 4T and CdS NPs take place in the blend. The nanoparticles are not well separated and tend to form clusters, suggesting the potential formation of efficient percolation pathways in the organic network.

3.3 Optical characterization of 4T and 4T:20 %[CdS] thin films

In Fig. 4, we present the absorption spectra of 4T and 4T:20 %[CdS] layers deposited on the glass substrate using spin coating technique. It appears that the incorporation of CdS NPs does not affect significantly the absorption of 4T which occurs in the UV visible range with a maximum of 383 nm corresponding to the HOMO–LUMO transition of pristine [26]. This is probably due to the low concentration (20 %) of CdS NPs in the organic matrix. In addition, the absorption coefficient of the NPs is much smaller than that of the organic matrix. However, the absence of any additional absorption peaks in the spectral range measured indicates that there is no significant ground-state charge transfer between the oligomer and the nanoparticles [27].

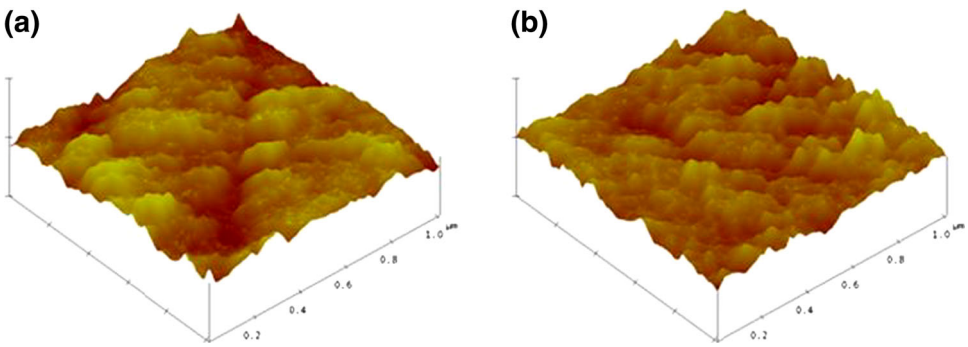

Fig. 3 AFM images of **a** 4T and **b** 4T : 20 %[CdS]

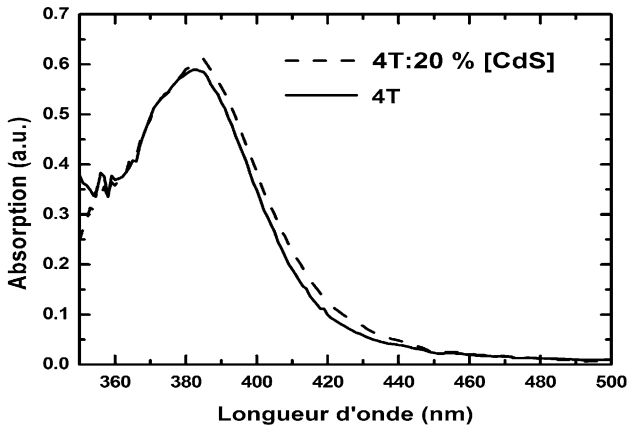

Fig. 4 Absorption spectra of 4T and 4T:20 %[CdS]

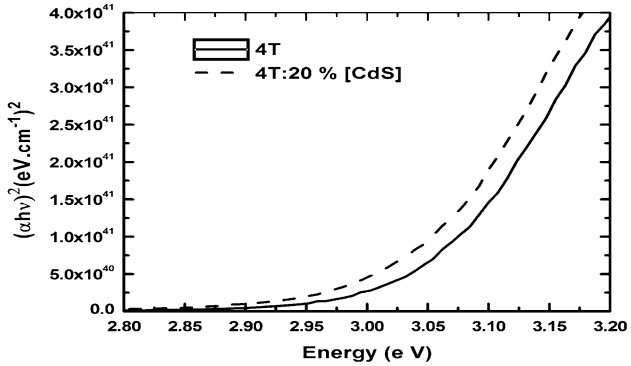

Fig. 5 Determination of optical energy gap of 4T and 4T:20 %[CdS]

From the absorption spectra, we can determine the band-gap energy of 4T and 4T/CdS layers by using the Tauc relation [28]:

$$(\alpha h\upsilon)^2 = C(h\upsilon - E_g) \quad (2)$$

where α is the optical absorption coefficient, h is the plank constant, υ is the frequency of excitation radiation, C is a characteristic constant of the materials, and E_g is the band gap. From the linear part of the $(\alpha h\upsilon)^2$ as a function of incident photon energy curve (Fig. 5), we get the optical band-gap energy E_g of 3.05 eV for 4T and 3.03 eV for 4T:CdS. The absorption band gap does not seem to be influenced by the CdS NPs incorporation. The band-gap energy value 3.05 eV obtained for 4T is of the same order than those reported previously in the literature [29].

Figure 6 shows the fluorescence spectra of 4T and 4T:20 %[CdS] layers. It clearly appears that the incorporation of CdS NPs does not strongly affect the shape of the spectrum but only reduces the fluorescence intensity of the pure oligomer; a significant quenching of organic compound emission is observed. The high intensity of 4T pristine luminescence is due to a low hole mobility and a short diffusion length of exciton [30].

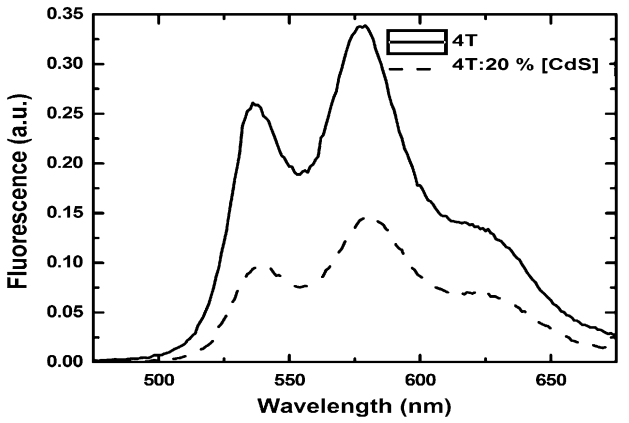

Fig. 6 Fluorescence spectra of 4T and 4T:20 %[CdS]

Moreover, the luminescence extinction provides an indication of the manner in which the two materials are mixed and the quality of the interface between them; the better CdS NPs are inserted in the oligomer, the more the luminescence of the latter is decreased which prevents their integration into the 4T network. The residual photoluminescence can be explained by assuming that phase separation between 4T and CdS NPs occurs on a length scale larger than the exciton diffusion length. In fact, the efficient quenching means that the singlet excitons can separate rapidly at the donor–acceptor interface.

Such quenching was observed in similar hybrid structures [31, 32]. In general, the recombination of electrons and holes occurs in the form of radiative and non-radiative decays of excitons during the diffusion and dissociation process (i.e., the presence of energy transfer from 4T to CdS NPs). This quenching phenomenon suggests that exciton decay via non-radiative transition can be attributed to charge transfer or energy transfer between the pristine and the CdS NPs. Indeed, excitons are essentially created in the 4T pristine through the photon absorption by this material. When they reach the interface formed by donor (4T) and the acceptor (CdS NPs), not only Forester resonance energy transfer (FRET) can occur but also charge-transfer process can occur. These transfer processes could cause the formation of hybrid excitons. The dissociation of these hybrid excitons in the inorganic–organic interface occurs, respectively, through three processes: (1) exciton formation in 4T, followed by electron transfer to CdS NPs; (2)exciton formation in 4T, followed by energy transfer to CdS NPs and then by hole transfer to 4T; and (3) exciton formation in CdS NPs, followed by hole transfer to 4T [33].

In the 4T:20 %[CdS] system, the excited electron can also move from the 4T to CdS NPs. This charge transfer leads to a decrease in the transition probability between the LUMO and HOMO orbital's simultaneously with a

quenching. Furthermore, the electrons from the oligomer fill the holes in CdS preventing and thus a direct electron–hole recombination, leading to the extinction of the emission of CdS nanoparticles.

3.4 Electrical characterization

3.4.1 Dark current and photocurrent

The external dark current as a function of applied voltage at room temperature for pristine (4T) and hybrid 4T:20 %[CdS] cells is shown in Fig. 7. In the 4T cell, the *J–V* plot shows two operating regimes: For low voltages, it exhibits ohmic behavior in which the current is proportional to the applied voltage. For medium voltages, one observes a space-charge-limited current (SCLC) with V^2 dependence [34]. In the hybrid cell, we observe, for higher voltage, a third operating regime in which the current behaves like V^n, $n = 3$. This regime is attributed to the trap-charge-limited current (TCLC) and could be ascribed to the effect of the interface area. The dark current in pure 4T is space charge limited allowing the direct determination of effective mobility from *J–V* measurements which is a combination of both electron and hole current. In fact, the ligand modifies the morphology of the active layers as they improve the compatibility between CdS NPs and 4T, leading to much more area interfaces between 4T and CdS NPs. Therefore, the exciton dissociation and the electrons transport between the two components are enhanced, and it generates the trap-charge-limited current. Therefore, there is a clear relationship between the film morphology and charge transport. In our 4T:20 %[CdS] blend, the mobility of electron is larger than hole mobility and hole diffusion lengths are shorter than the thickness of active layer. As a consequence, the holes will accumulate in the device than electrons, which makes the applied field non-uniform. As a result of this, the electric field increases in the region near to the anode, enhancing the extraction of holes. Conversely, in the region near the cathode, the electric field decreases, diminishing the extraction of electrons. It is evident that in the region near to the anode, the accumulated holes are not neutralized by an equal density of electrons.

3.4.2 Photovoltaic parameters

Photocurrent generation in the bulk heterojunction devices is governed by a number of processes:

- The generation of excitons after the absorption of light by organic component
- The exciton diffusion toward the organic–inorganic interface area
- The dissociation in free charge carriers via charge transfer or energy transfer

After dissociation, a germinate pair of a hole and an electron is formed. The bound e–h pairs must dissociate into free charge carriers and subsequently move to the electrodes. The *J–V* curves under white light illumination through the ITO side for cells based on pristine 4T and hybrid 4T:20 %[CdS] are shown in Fig. 8.

We obtain a significantly high photocurrent. Nevertheless, the striking difference between the two samples is upon the huge variation of the photocurrent as a function of applied. As it is clearly seen in Fig. 8, one can assert that incorporation of CdS nanoparticles in the 4T layer increases the cell performances. One can notice that incorporation of CdS nanoparticles in the 4T layer leads to an increase in the photocurrent J and also induces an increase in the photovoltaic parameters such as open-circuit voltage (V_{oc}), short-circuit current density (J_{sc}), fill factor (FF), conversion efficiency (η), and therefore cell

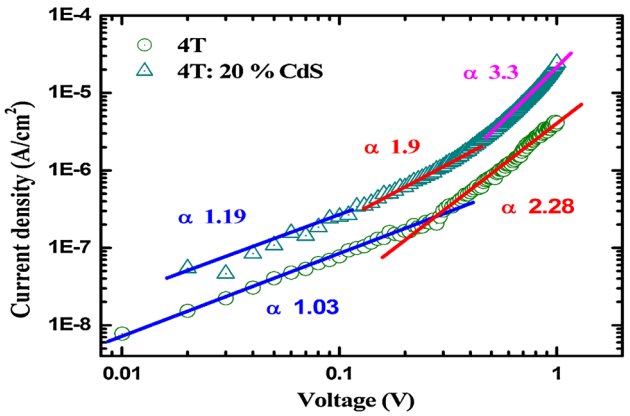

Fig. 7 Current density versus applied voltage in dark (logarithmic scale)

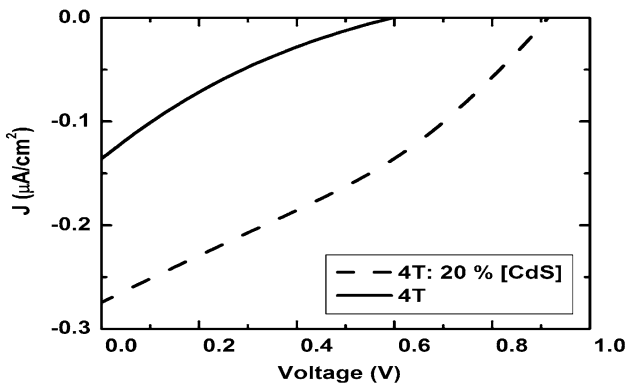

Fig. 8 *J–V* characteristics under illumination of 4T and 4T:20 %[CdS]

Table 1 Key photovoltaic parameters extracted from *J–V* characteristics from 4T and 4T:20 %[CdS] cells

Cell	V_{OC} (V)	J_{SC} (mA cm^{-2})	FF	$\eta \times 10^{-2}$ (%)
4T	0.81	0.15	0.15	0.91
4T:20 %[CdS]	0.92	0.27	0.34	4.22

performances. The values of these parameters are summarized in Table 1.

It is clear that the efficiency reported here is lower than that reported by other authors. For example, Wang et al. [35] reported an even higher efficiency of 1.17 % using multiarmed CdS nanorods/MEH-PPV solar cells. The main reason for the low efficiency of many devices is the low value of J_{sc} which is affected by optical absorption properties, the thickness of active layer, the interface, and the band-gap matching of the materials [36]. Figure 8 shows the presence of S-shaped behavior in the *J–V* curve [37, 38]. For the 4T pristine, this could be lead to the poor Al/4T pristine contact which could be explained by the rapid vacuum evaporation of aluminum and the high roughness and porosity of 4T pristine layer. The hybrid 4T:20 %[CdS] *J–V* curve shows the absence of the S-shaped curve, and this phenomenon could be related to the modified Braun–Onsager theory. The modification of the feature may be accounted for by the difference in photogeneration efficiency between the two kinds of samples; indeed, the dissociation probability $P\prime(E)$ given in Eq. (9) has a slower variation than $P(E)$ in Eq. (3) [39, 40], as more discussed below.

The low fill factor could be attributed to the organic ligand at the surface of CdS NPs and the poor electrical contact with the metallic electrode due to surface roughness. This may be caused also by the large spaces between the CdS NPs and NPs-oligothiophene in the blend film [24].

The conversion efficiency η of 4T:20 %[CdS] cell is approximately five times higher than η of the pristine 4T cell. This is mainly due to the incorporation of CdS nanoparticles in the organic matrix which increases significantly the conversion efficiency of the photovoltaic cell. The enhancement of photovoltaic parameters in the case of our BHJ cell results from the wide interface area between organic (4T) and inorganic (CdS NPs) phases. The enhancement of the junction area favors the dissociation of those tightly bound Frenkel excitons photogenerated in the organic matrix (4T), leading to higher photocurrent values. After the electron transfer at the donor/acceptor interface and the subsequent dissociation, the electrons are localized in the CdS NPs phase, whereas the holes remain in the 4T chains. Subsequently, the free electrons and holes must be transported via percolated CdS NPs and 4T pathways toward the electrodes to produce the photocurrent in the device. Indeed, the hybrid mixture consists of two components having different electron affinities and ionization potentials; electron will be transferred to the constituent of greater electron affinity, whereas the hole will migrate to the constituent of lowest ionization potential. The photocurrent density j_{ph} is obtained by subtracting the dark current from recorded current under illumination, and effective potential $V_{bi} - V$ is provided from the effective electric field in the bulk which results from algebraic sum of the built-in field (E_{bi}) and the applied field E [39]. The photocurrent in BHJ photovoltaic cells is dominated by the dissociation efficiency of bound electron hole pairs at the donor acceptor interface. Therefore, the electron transport in CdS NPs and the hole transport in 4T are crucial for the understanding the electronic and optoelectronic properties of bulk heterojunction photovoltaic devices. Others free electrons can contribute to the photocurrent, after being dissociated from the exciton at the interface, due to the increased number of percolation pathways.

3.4.3 *The Braun–Onsager theory*

The Braun–Onsager theory is widely used to explain exciton dissociation in organic semiconductors. Onsager explained the photogeneration of free charge carriers in low mobility materials (such as organic materials) by the germinate recombination theory, and he used to calculate the probability to separate a Coulomb-bound electron–hole pair with a given initial distance under the action of an external electric field [41]. Later, Braun extended this theory; he applied the initial separation distance of the geminate electron–hole pairs to the charge-transfer exciton states [42]. The dissociation probability $P(E)$ given by Braun is:

$$P(E) = \frac{k_d(E)}{k_d(E) + k_f} \tag{3}$$

here, E is the effective electric field and $k_f = \tau^{-1}$ is the recombination rate of the geminate pair; the field dependent dissociation rate $k_d(E)$ is given by:

$$k_d(E) = \frac{3\gamma}{4\pi r_{gp}^3} \exp - \left(\frac{E_b}{k_B T}\right) \frac{J_1(2\sqrt{-2b})}{\sqrt{-2b}} \tag{4}$$

where $\gamma = q\mu/\varepsilon\varepsilon_0$ is the Langevin recombination factor, μ the sum of electron and hole charge carrier mobilities, r_s is the initial geminate pair radius, $k_B T$ is the thermal energy, E_b is the binding energy of the geminate pair, J_1 is the first order Bessel function, e is the elementary charge, and $\varepsilon\varepsilon_0$ is the effective permittivity of the organic semiconductor and $b = \frac{e^3 E}{8\pi\varepsilon\varepsilon_0 (k_B T)^2}$.

According to the Braun–Onsager model (BO), the photocurrent can be written as:

$$j_{\mathrm{ph,BO}} = eG_{\max}P(E)h \tag{5}$$

where $G_{\max}$ is the maximum generation rate of free carriers, $P(E)$ is the probability for charge separation at the donor–acceptor interface, and h is the device thickness. Another important factor that can affect the photocurrent in BHJ is the charge carrier extraction: Free charge carriers that do not recombine can be extracted from the device and also contribute to the photocurrent. Sokel and Hughes have developed an analytical model with several simplifying assumptions such as neglecting recombination, trapping, and infinite surface recombination velocity [43]. The photocurrent expression is thus given by [44]:

$$j_{\mathrm{ph,SH}} = j_{ph,\max}\left(\frac{\exp(eV/k_BT)+1}{\exp(eV/k_BT)-1} - \frac{2k_BT}{e}\right) \tag{6}$$

where $J_{\mathrm{ph,max}} = eGh$, J is the maximum photocurrent with G as the generation rate of free charges in the active layer, L is the device thickness, k_BT/e is the thermal voltage, and V is the internal voltage. Mihailetchi et al. [40] described the photocurrent of a BHJ photovoltaic cell by combining the charge diffusion term in the Sokel–Hughes model to a dissociation charges term based on the Braun–Onsager description. Thus, the final photocurrent can be written as:

$$j_{\mathrm{ph}} = j_{\mathrm{ph,BO}}\left(\frac{\exp(eV/k_BT)+1}{\exp(eV/k_BT)-1} - \frac{2k_BT}{e}\right) \tag{7}$$

$$j_{\mathrm{ph}} = eG_{\max}P(E)h\left(\frac{\exp(eV/k_BT)+1}{\exp(eV/k_BT)-1} - \frac{2k_BT}{e}\right) \tag{8}$$

We use Eq. (8) to analyze the photocurrent for the 4T pristine and the hybrid 4T:20 %[CdS]. In Fig. 9a, we apply the last combination to fit experimental data for an initial electron–hole pair separation $r_{\mathrm{gp}} = 0.3$ nm, a maximum generation rate $G_{\max} = 2.710^{27}$, a thickness of organic layer $h = 200$ nm, a decay rate $k_f = 1.4\ 10^{-5}\ \mathrm{s}^{-1}$, and dielectric constant $\varepsilon = 3$ (see Fig. 9b).

On the other side, bulk heterojunction (BHJ) 4T:20 %[CdS] needs another parameter to account for the enhancement of effective current versus effective potential as compared to pristine 4T cell.

This would suggest an addition probability term labeled k_i that takes into account the exciton dissociation on the interface 4T:20 %[CdS]. We assume that k_i is constant and proportional to the interface area of 4T:20 %[CdS].

In Fig. 10a, we apply the same combination as for the former Fig. 9a, but in this case, we consider the dissociation constant k_i in the total probability of dissociation:

$$P'(E) = \frac{k_d(E)+k_i}{k_d(E)+k_i+k_f} \tag{9}$$

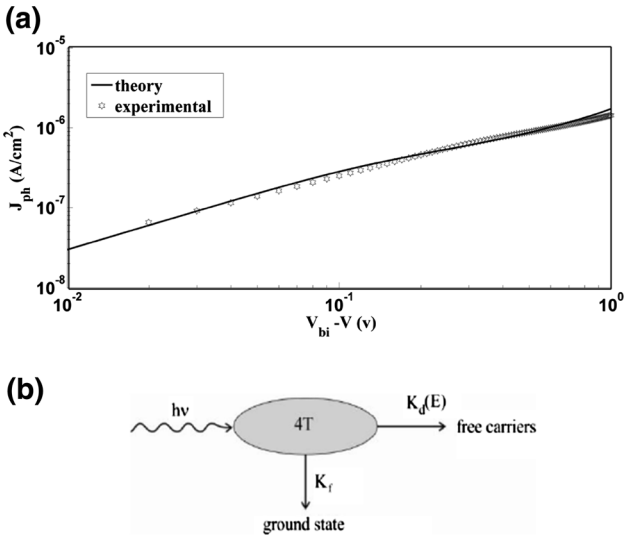

Fig. 9 **a** Effective photocurrent versus effective potential, open circles show the experimental data of pristine 4T, and the solid line shows the MATLAB calculation according to Eq. (3). **b** Schematic model of photogeneration in pristine 4T

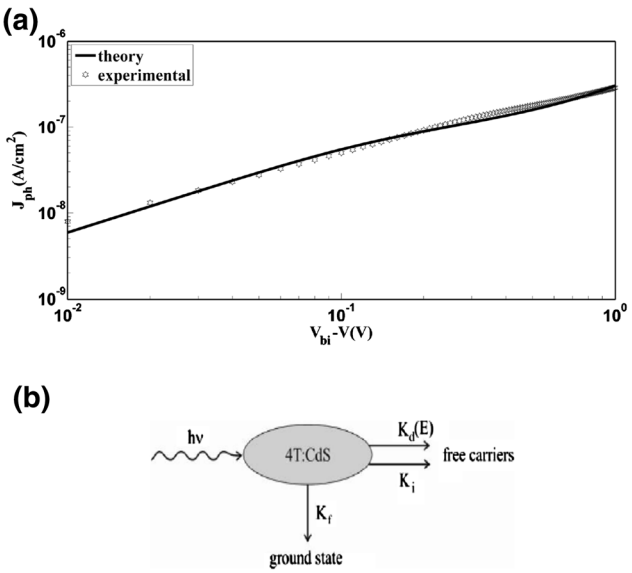

Fig. 10 **a** Effective photocurrent versus effective potential, open circles show the experimental data of 4T:20 %[CdS], and the solid line shows the MATLAB calculation according to Eq. (9). **b** Schematic model of photogeneration in 4T:20 %[CdS]

Consequently, the new expression of effective photocurrent is written as:

$$j'_{\mathrm{ph}} = eG_{\max}P'(E)h\left(\frac{\exp(eV/k_BT)+1}{\exp(eV/k_BT)-1} - \frac{2k_BT}{e}\right) \tag{10}$$

The best fit to the experimental photocurrent, considering the new expression $P'(E)$, was obtained for $k_i = 2.2\ 10^{-15}\ \mathrm{s}^{-1}$. All the other parameters were identical to the former case (see Fig. 10b).

The organic/inorganic surface area governs the kinetics of our hybrid layer and favors the charge process dissociation. Our results depict the important effect of the surface area in the photocurrent. It is well established that the dissociation of photocreated excitons occurs preferentially at the organic/inorganic interface [45]. However, it turns out that the area of the interface 4T:20 %[CdS] can play an important role in the process of photogeneration of free carriers in such a nanocomposite structure. In a classical scheme where the hybrid solar cell junction is made of a flat contact between the mineral and the organic semiconductor, the interface area of that junction equals that of the active pixel, whereas in a bulk heterojunction structure like our case, the interface area S, which is written as $S = S_{NP} \times N_{NP}$, where S_{NP} is the surface area of spherical nanoparticles and N_{NP} is the number of nanoparticles in the sample, is obtained from the relation $m_T = m_{NP} \times N_{NP}$, where m_T the total is mass of CdS nanoparticles (2 mg), m_{NP} is the mass of one CdS nanoparticle, and m_{NP} is given by $m_{NP} = d_{CdS} \times V_{NP}$, where$d_{CdS}$ is the bulk density of CdS (4.826 g cm^{-3}) and V_{NP} is the volume of one CdS nanoparticle ($V_{NP} = 1.2 \times 10^{-19}$ cm^3); according to this, we find $m_{NP} = 5.8 \times 10^{-19}$ s and $N_{NP} = 3.4 \times 10^{15}$. Finally, the value of S is 0.38 m^2. Nonetheless, this is only an approximate value since in our calculation we assumed monodisperse spherical non-aggregated nanoparticles. The interface area is larger than the effective area of the sample (2 cm^2). This value states that the incorporation of nanoparticles in the organic matrix increases the organic/inorganic interface area and therefore promotes the exciton dissociation and consequently photovoltaic current. We can conclude that bulk heterojunction greatly increases interfacial area between donor and acceptor materials, which enables charge separation within the bulk instead of just at the planer interface of a simple bilayer.

4 Conclusion

We have realized hybrid photovoltaic cells by incorporating CdS nanoparticles in an organic matrix of quaterthiophene. From the fluorescence spectra, it appears that CdS nanoparticles act as quenching centers, suggesting that the bulk heterojunction structure is more favorable to photovoltaic conversion. A modified Braun–Onsager model was used for the hybrid structure (4T:20 %[CdS]) photocurrent study, suggesting that it results from the contribution of the dissociation of photogenerated excitons in the organic phase ($k_d(E)$) and their ionization through the interaction with the CdS nanoparticles (k_i). In addition, this model could explain successfully the comprehension of charge transport kinetic in hybrid solar cell devices. The conversion efficiency of the hybrid 4T:20 %[CdS] cells is approximately five times higher than that of pristine 4T. This clearly asserts that hybrid cells may constitute a promising alternative to increase the performances of organic photovoltaic cells.

References

1. T. Toccoli, M. Tonezzer, P. Bettotti, N. Coppedè, S. Larcheri, A. Pallaoro, L. Pavesi, S. Iannotta, Org. Electron. **10**, 521–526 (2009)
2. K. Takimiya, Y. Kunugi, T. Otsubo, Chem. Lett. **36**, 578 (2007)
3. M.A. Saidani, A. Benfredj, S. Romdhane, F. Kouki, H. Bouchriha, Phys. Rev. B **86**, 165315 (2012)
4. B.R. Saunders, M.L. Turner, Adv. Colloid Interface Sci. **138**, 1–23 (2008)
5. C. Barone, G. Landi, A. DeSio, H.C. Neitzert, S. Pagano, Sol. Energy Mater. Sol. Cells **122**, 40–45 (2014)
6. C. Reanprayoon, J. Gasiorowski, M. Sukwattanasinitt, N.S. Sariciftci, P. Thamyongkit, RSC Adv. **4**, 3045–3050 (2014)
7. V.I. Boev, A. Soloviev, C.J.R. Silva, M.J.M. Gomes, Solid State Sci. **8**, 50–58 (2006)
8. Y. Zhou, F.S. Riehle, Y. Yuan, H.-F. Schleiermacher, M. Niggemann, G.A. Urban, M. Krüger, App. Phy. Lett. **96**, 013304 (2010)
9. D. Yun, W. Feng, H. Wu, K. Yoshino, Sol. Energy Mater. Sol. Cells **93**, 1208–1213 (2009)
10. S. Jaziri, S. Romdhane, H. Bouchriha, R. Bennaceur, Phys. Lett. A **234**, 141–146 (1997)
11. J. Yang, A. Tang, R. Zhou, J. Xue, Sol. Energy Mater. Sol. Cells **95**, 476–482 (2011)
12. S. Shiojiri, T. Hirai, I. Komasawa, J. Chem. Eng. Jap. **30**, 86 (1997)
13. S. Kango, S. Kalia, A. Celli, J. Njuguna, Y. Habibi, R. Kumar, Prog. Polym. Sci. **38**, 1232–1261 (2013)
14. N. Mastour, Z.B. Hamed, A. Benchaabane, M.A. Sanhoury, F. Kouki, Org. Electron. **14**, 2093–2100 (2013)
15. A. Agostiano, M. Catalano, M.L. Curri, M. Della Monica, L. Manna, L. Vasanelli, Micron **31**, 253–258 (2000)
16. N.B.H. Mohamed, M. Haouari, N. Jaballah, A. Bchetnia, K. Hriz, M. Majdoub, H.B. Ouada, Phys. B Condens. Matter **407**, 3849–3855 (2012)
17. S. Shiojiri, T. Hirai, I. Komasawa, J. Chem. Eng. Jpn. **30**, 86 (1997)
18. M. Curri, A. Agostiano, L. Manna, M.D. Monica, M. Catalano, L. Chiavarone, V. Spagnolo, M. Lugara, J. Phys. Chem. B. **104**, 8391 (2000)
19. W.W. Yu, L. Qu, W. Guo, X. Peng, Chem. Mater. **15**, 2854–2860 (2003)
20. S.K. Mishra, R.K. Srivastava, S.G. Prakash, R.S. Yadav, A.C. Panday, J Electron. Mater. Lett. **7**, 31 (2011)
21. N. Pinna, K. Weiss, J. Urban, M. Pileni, Adv. Mater. **13**, 261 (2001)
22. L. Wang, Y.S. Liu, X. Jiang, D.H. Qin, Y. Cao, J. Phys. Chem. C **111**, 9538 (2007)
23. J.P. de Carvalho Alves, J.N. de Freitas, T.D.Z. Atvars, A. Flávia Nogueira, Synth. Met. **164**, 69 (2013)
24. X. Jiang, F. Chen, W. Qiu, Q. Yan, Y. Nan, H. Xu, L. Yang, H. Chen, Sol. Energy Mater. Sol. Cells **94**, 2223 (2010)
25. Z.B. Hamed, A. Benchaabane, F. Kouki, M.A. Sanhoury, H. Bouchriha, Synth. Met. **195**, 102–109 (2014)

26. M.A. Saidani, A. Benfredj, F. Kouki, S. Romdhane, J.L. Fave, H. Bouchriha, Synth. Met. **162**, 1746–1749 (2012)
27. N.C. Greenham, X. Peng, A.P. Alivisatos, Phys. Rev. B **54**(24), 17628 (1996)
28. Q. Gul, M. Zakria, T.M. Khan, A. Mahmood, A. Iqbal, Mater. Sci. Semicond. Process. **19**, 17–23 (2014)
29. D. Fichou, G. Horowitz, B. Xu, F. Gamier, Synth. Met. **48**, 167–179 (1992)
30. Y. Liu, L.Y. Wang, Y. Cao, Front. Chem. Chin. **2**, 383 (2007)
31. D. Deng, M. Shi, F. Chen, L. Chen, X. Jiang, H. Chen, Sol. Energy **84**, 771–776 (2010)
32. C. Greeham, X. Peng, A.P. Alivisatos, Phys. Rev. B **54**, 17628–17637 (1996)
33. S.N. Sharm, T. Vats, N. Dhenadhayalan, P. Ramamurthy, A.K. Narula, Sol. Energy Mater. Sol. Cells **100**, 6–15 (2012)
34. F. Schauer, Sol. Energy Mater. Sol. Cells **87**, 235–250 (2005)
35. L. Wang, Y.S. Liu, X. Jiang, D.H. Qin, Y. Cao, J. Phys. Chem. C **111**, 9538 (2007)
36. J. Rostalski, D. Meissner, Sol. Energy Mater. Sol. Cells **63**, 37 (2000)
37. D. Gupta, M. Bag, K.S. Narayan, Appl. Phys. Lett. **92**, 093301 (2008)
38. A. Kumar, S. Sista, Y. Yang, J. Appl. Phys. **105**, 094512 (2009)
39. F. Kouki, G. Horowitz, F. Garnier, H. Bouchriha, Org. Electron. **11**, 1439–1444 (2010)
40. V.D. Mihailetchi, L.J.A. Koster, J.C. Hummelen, P.W.M. Blom, Phys. Rev. Lett. **93**, 6601 (2004)
41. L. Onsager, Phys. Rev. **54**, 554–557 (1938)
42. C.L. Braun, J. Chem. Phys. **80**, 4157 (1984)
43. J.C. Scott, G.G. Malliaras, Chem. Phys. Lett. **299**, 115–119 (1999)
44. R. Sokel, R.C. Hughes, J. Appl. Phys. **53**, 7414 (1982)
45. D. Yun, W. Feng, H. Wu, K. Yoshino, Sol. Energy Mater. Sol. Cells **93**, 1208–1213 (2009)